LETTERS
PUBLISHED ONLINE: 22 APRIL 2012 | DOI: 10.1038/NGEO1454

nature geoscience

Variations in earthquake rupture properties along the Gofar transform fault, East Pacific Rise

Jeffrey J. McGuire[1]*, John A. Collins[1], Pierre Gouédard[2], Emily Roland[3†], Dan Lizarralde[1], Margaret S. Boettcher[4], Mark D. Behn[1] and Robert D. van der Hilst[2]

On a global scale, seismicity on oceanic transform faults that link mid-ocean ridge segments is thermally controlled[1,2]. However, temperature cannot be the only control because the largest earthquakes on oceanic transform faults rupture only a small fraction of the area that thermal models predict to be capable of rupture[3–5]. Instead, most slip occurs without producing large earthquakes[3,4,6]. When large earthquakes do occur, they often repeat quasiperiodically[7,8]. Moreover, oceanic transform faults produce an order of magnitude more foreshocks than continental strike-slip faults[7,9]. Here we analyse a swarm of about 20,000 foreshocks, recorded on an array of ocean-bottom seismometers, which occurred before a magnitude 6.0 earthquake on the Gofar transform fault, East Pacific Rise. We find that the week-long foreshock sequence was confined to a 10-km-long region that subsequently acted as a barrier to rupture during the mainshock. The foreshock zone is associated with a high porosity and undergoes a 3% decrease in average shear-wave speed during the week preceding the mainshock. We conclude that the material properties of fault segments capable of rupturing in large earthquakes differ from those of barrier regions, possibly as a result of enhanced fluid circulation within the latter. We suggest that along-strike variations in fault zone material properties can help explain the abundance of foreshocks and the relative lack of large earthquakes that occur on mid-ocean ridge transform faults.

The short (~90 km), high-slip-rate (~14 cm yr^{-1}) Gofar transform fault[10] on the equatorial East Pacific Rise (EPR; Fig. 1) has a warm thermal structure, which limits its largest earthquakes to $6.0 \leq M_w \leq 6.2$, where M_w is the moment magnitude. These magnitude (M) 6.0 earthquakes repeat quasiperiodically approximately every five to six years[7] (Supplementary Fig. S1). The westernmost segment of the Gofar transform fault has two asperities that have ruptured repeatedly in $M \sim 6.0$ earthquakes (Fig. 1; Supplementary Fig. S1). The eastern asperity (centred on the blue circle in Fig. 1) ruptured in 1997, 2002 and 2007, whereas the western asperity (centred on the orange circle in Fig. 1) ruptured in 1992, 1997, 2003 and 2008 (refs 7,8). These fully coupled fault patches[8] are anomalous relative to the dominant behaviour of mid-ocean ridge transform faults (RTFs) where 80% of fault motion occurs without earthquakes[3,4]. The repeating large ruptures present an opportunity to understand the physical processes that produce the high rates of RTF foreshock activity and limit the size of RTF ruptures to be much smaller than the full fault length[9,11].

Based on the regularity of EPR seismic cycles, we deployed an ocean bottom seismograph (OBS) array to capture the 2008 M_w 6.0 Gofar earthquake as well as its foreshocks and aftershocks. Seven OBSs, each with a strong-motion accelerometer and a broadband seismometer, were deployed on the western asperity (Fig. 1), which ruptured on 18 September 2008 in a M_w 6.0 earthquake. The entire earthquake sequence was recorded on scale by the strong-motion network, providing an unprecedented data set covering the end of the seismic cycle on an RTF.

During 2007–2008, the Gofar fault failed in a series of ruptures that propagated from east to west. Figure 1 shows the epicentres of nearly 22,000 earthquakes between 1 August and 30 December 2008 relocated with waveform-derived differential arrival times (see Methods). The 2007 M 6.0 rupture zone (~105.7°–105.9° W) experienced a low rate of seismicity throughout our deployment in 2008 (Fig. 2); in contrast, the area immediately west experienced a high rate of seismicity between 1 January and 1 September (yellow region in Fig. 2) culminating in a spectacular swarm of ~20,000 foreshocks from 10 September (day 254) to 17 September (day 261). The foreshock swarm was effectively terminated on 18 September (day 262) by the rupture of the M 6.0 mainshock on the segment directly to the west (red region in Fig. 2). The westernmost ~10 km of the plate boundary (106.2°–106.3° W) failed in another swarm of ~20,000 earthquakes on 10–17 December (cyan in Figs 1, 2; Supplementary Figs S2 and S3) to complete the seismic cycle. The fault segments hosting the foreshock and December swarm have little overlap with the mainshock rupture zone as delineated by its immediate aftershocks (Figs 1 and 2).

Two observations indicate that the physical properties in the swarm/foreshock regions differ from those in the M 6.0 rupture zones. First, large ruptures generally fail to propagate through the foreshock region. Since 1992, seven $M \geq 6.0$ ruptures have occurred on the western Gofar fault, all of which have centroids at either the eastern or western asperity[7,8] (Fig. 1 and Supplementary Fig. S1) and have rupture lengths of ~15–20 km based on the distribution of 2008 aftershocks. None of these large ruptures propagated through the 2008 foreshock region to rupture both asperities, despite the near synchronization of their seismic cycles (Supplementary Fig. S1) and the apparent continuity of the fault (fault offsets are <2 km based on earthquake locations and bathymetry). This historical behaviour, together with the sharp boundary observed between the 2008 foreshocks and aftershocks (Fig. 2 and Supplementary Fig. S3), indicates that a region with distinct mechanical properties separates the M 6.0 ruptures of the eastern and western asperities (Fig. 1) and thereby limits earthquake magnitude along this RTF. The ability of the foreshock region to repeatedly stop M 6.0 rupture fronts, despite being only ~10 km long, indicates that this barrier

[1]Department of Geology and Geophysics, Woods Hole Oceanographic Institution, Woods Hole, Massachusetts 02543, USA, [2]Department of Earth, Atmospheric, and Planetary Sciences, Massachusetts Institute of Technology, Cambridge, Massachusetts 02139, USA, [3]MIT-WHOI Joint Program, Massachusetts Institute of Technology, Cambridge, Massachusetts 02139, USA, [4]University of New Hampshire, Department of Earth Sciences, Durham, New Hampshire 03824, USA. [†]Present address: US Geological Survey, Anchorage, Alaska 99508, USA. *e-mail: jmcguire@whoi.edu.

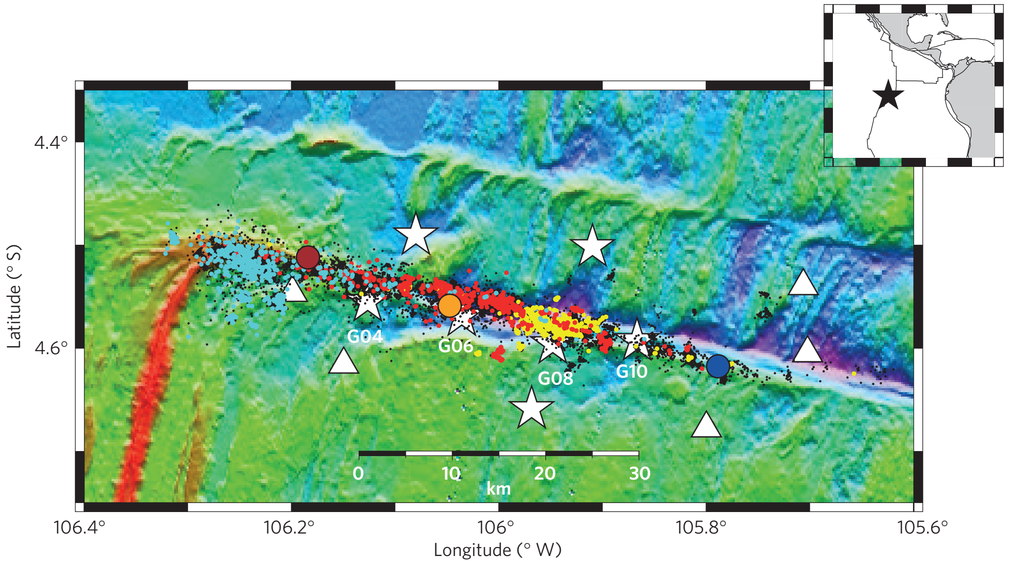

Figure 1 | Earthquake epicentres at the Gofar transform fault. The bathymetry map (the location of which is indicated by the black star on the inset) shows 21,919 events occurring in August–December 2008 (black dots) and located with a double-difference scheme. Foreshocks on 10–12 September, aftershocks on 18–20 September and swarm events on 7–8 December are shown in yellow, red and cyan, respectively. OBS locations are shown by the white triangles (seismometer only) and white stars (seismometer plus strong-motion sensor). The epicentre of the largest (M 5.2) aftershock and the centroids of the 2008 M_w 6.0 and 2007 M_w 6.2 earthquakes are shown as large brown, orange and blue circles, respectively. OBS G04, G06, G08 and G10 are labelled below their symbols.

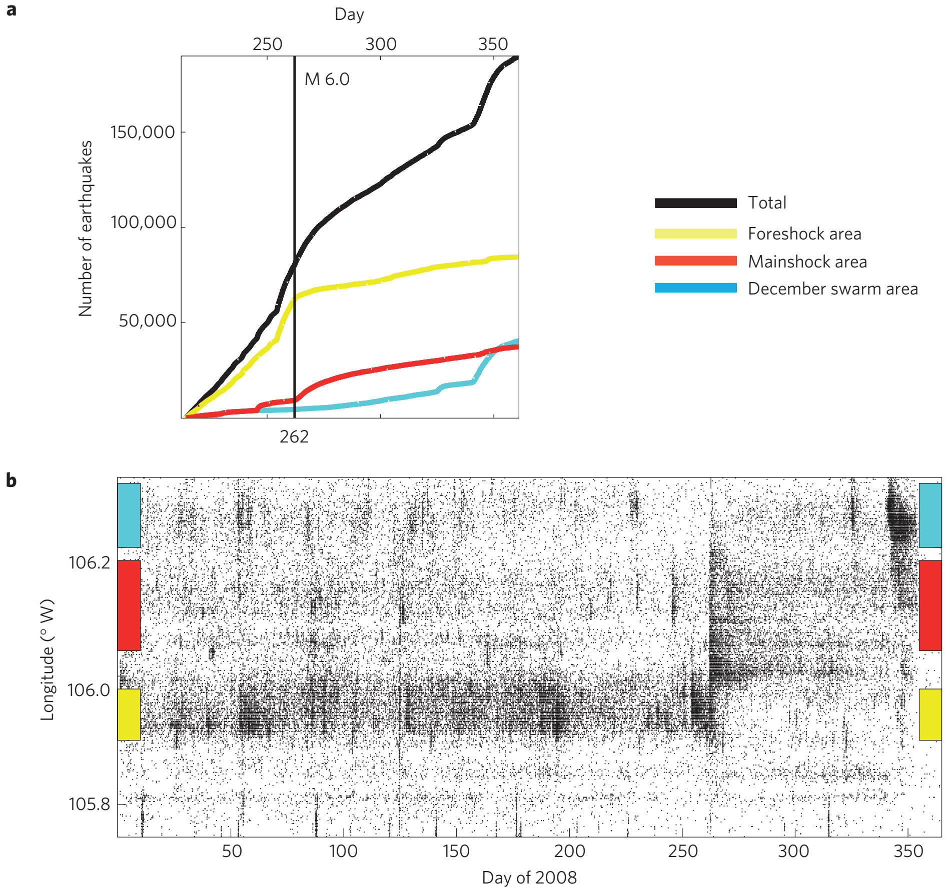

Figure 2 | Earthquake temporal distribution. a, Cumulative number of earthquakes in the waveform-detection earthquake catalogue (black curve). The yellow, red and cyan curves show cumulative earthquakes in the foreshock zone (105.9°–105.98° W), mainshock rupture zone (106.04°–106.18° W) and the December swarm zone (106.2°–106.3° W), respectively. The M 6.0 mainshock occurred on day 262, or 18 September (vertical black line). **b**, Locations and times of all of the earthquakes in the STA/LTA catalog covering the entire year of 2008. The solid yellow, red and cyan rectangles denote the same sections of the fault as the coloured curves in **a**.

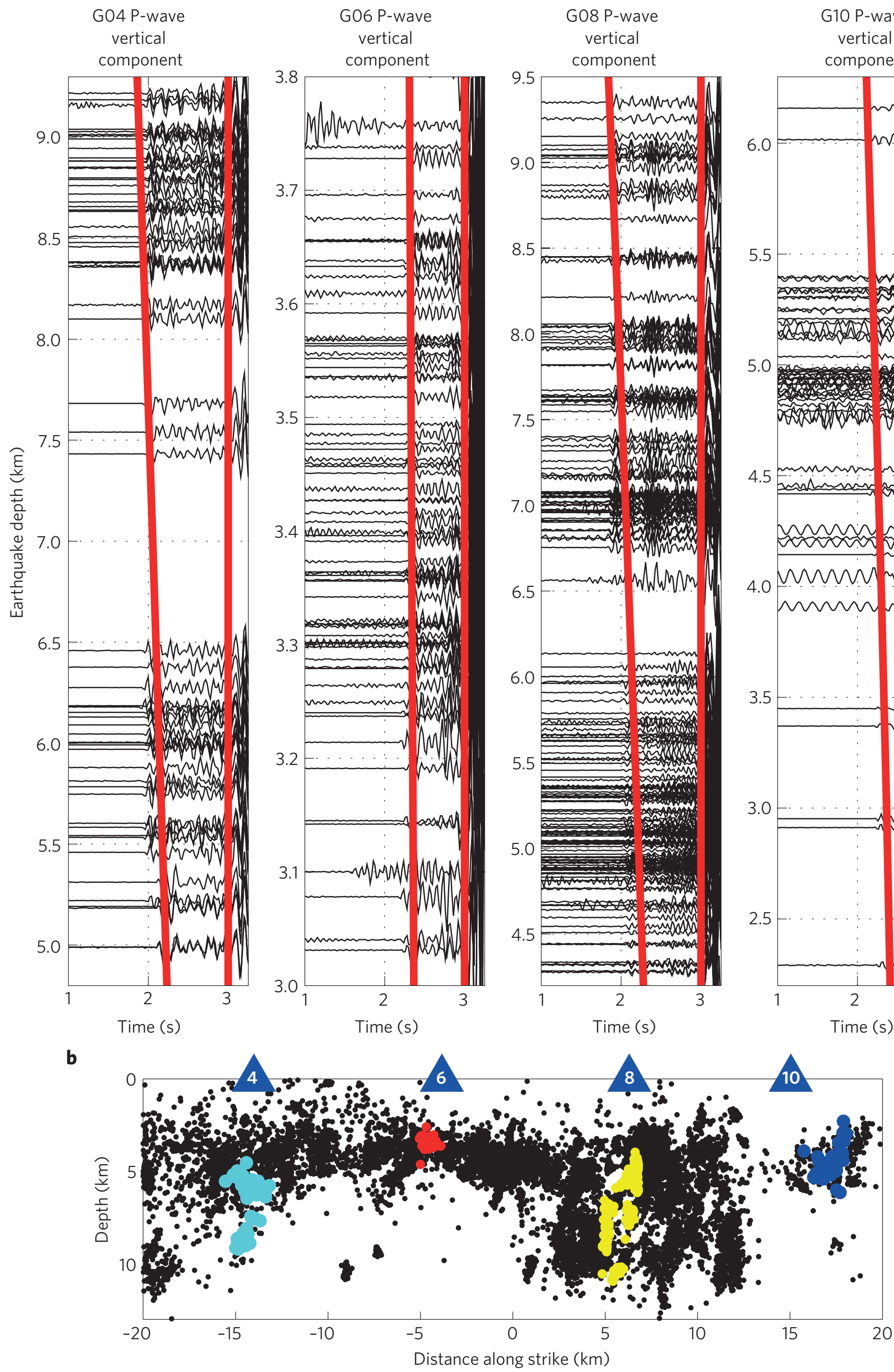

Figure 3 | Along-strike variations in earthquake depths. a, Vertical-component P waveforms for clusters of earthquakes directly beneath each fault-zone station as a function of hypocentral depth. The waveforms are aligned with S-wave first arrivals at 3.0 s. These clusters are located within 1–3 km epicentral distance and hence are dominantly vertically propagating rays. The observed S-wave first-arrival time (vertical red line at 3.0 s) and the predicted P-wave arrival time (earlier red line) from a fault-zone velocity model[14] that assumes a V_p/V_s ratio of 1.73 are shown. Note the significant difference in the maximum S–P time between stations in the rupture zones of M 6.0 earthquakes (G06 ∼0.8 s, G10 ∼0.7 s) and those in the swarm/foreshock zones (G08 ∼1.25 s, G04 ∼1.1 s). **b**, Relocated seismicity with cyan, red, yellow and blue circles denoting the clusters beneath stations G04, G06, G08 and G10 (blue triangles), respectively.

comprises strongly velocity-strengthening frictional material[12] that is not present in the adjacent M 6.0 rupture zones.

Second, microearthquakes in the barrier region extend a few kilometres into the uppermost mantle, in contrast to the crust-confined events within the mainshock rupture zone (Fig. 3). Vertically propagating S waves within the fault zone arrive ∼1.25 s after the P wave for deep foreshocks and December swarm events (beneath stations G08 and G04, respectively), whereas the maximum S–P times for events in the M 6.0 rupture zones (G06 and G10) are ∼0.6–0.8 s (Fig. 3). This difference seems to result primarily from variations in earthquake depth along the fault rather than from lateral heterogeneities in crustal velocity structure.

We cannot exclude the possibility that some of the difference in S–P times results from along-strike anomalies in the ratio of the P-wave velocity to the S-wave velocity (V_p/V_s ratio) but the V_p/V_s ratio in the lower crust of the foreshock region seems typical of oceanic crust (Supplementary Fig. S4) and we conclude that most of the difference in S–P times results from deeper events in the foreshock region (see Supplementary Methods). Oceanic earthquakes are generally confined to depths shallower than the 600 °C isotherm[13]. For a half-space cooling model, this depth is ~4 km in the centre of the Gofar transform and would increase to only 5–6 km for thermal models[5] that include hydrothermal cooling. Thus, the depth extent of seismicity in the mainshock regions is consistent with these thermal/rheological models, but the deeper seismicity in the foreshock zone (~7–10 km; Fig. 3) is not.

Subtle changes in waveforms from earthquakes directly underneath station G08 indicate that the elastic properties of the rupture-barrier region changed during the foreshock swarm. We inferred such medium changes, represented as relative changes (dv/v) in S-wave speed, from the time-dependent stretching of the S-wave coda (Fig. 4) measured with a doublet method[10] (see Methods). For each selected earthquake we determined a stretching coefficient by comparison against a reference signal, which was obtained by stacking waveforms from selected small earthquakes that occurred in the foreshock region before day 240 (Fig. 4). The dense foreshock sequence allowed for continuous monitoring of S-wave speed variations through the mainshock on day 262.

We found a ~3% decrease in S-wave speed in the fault zone during the foreshock swarm well before the mainshock (Fig. 4). An active-source refraction study through the foreshock zone found a few-kilometres-wide zone of low P-wave velocities around the active fault that extends throughout the crust[14]. Our coda measurements are probably most sensitive to the shallow (~0–3 km) part of the damage zone where the P-wave speed anomaly is greatest (~30%; ref. 14). The change in elasticity seems to be limited to the foreshock zone, as waveforms from the same set of earthquakes recorded at stations located east (G10) or west (G06) of that zone do not indicate such a time dependence (Supplementary Fig. S5). If the temporal changes represent the response of fluid-filled cracks to a change in stress, the minimum stress change would be about 0.03 MPa (stress sensitivity of 10^{-6}), but it could be one to two orders of magnitude larger[15]. Estimating stress changes from reductions in seismic-wave speed may be inaccurate, however, because: first, the elastic response may not be linear; second, the wave-speed reduction was transient (Fig. 4) unlike the expected static stress change from a creep event; and third, the velocity reduction correlated with seismicity rate, which during creep events is expected to be a function of stressing rate, not stress[16]. A similar correlation between stressing rate and wave-speed change has been observed for a large slow-slip event in the Guerrero subduction zone, implying nonlinear elasticity effects[17].

Generating the inferred stress change over a significant portion of the fault is likely to require a deformation event larger than the biggest foreshock (M_w 4.1). Such a slip event would have been primarily aseismic, similar to other earthquake swarms triggered by creep events[11,18]. Although no seafloor geodetic data are available for the Gofar fault, collectively, our observations indicate that both the foreshock swarm and the changes in seismic wave speed resulted from the increased stressing rates caused by a large aseismic creep event that occurred within the rupture-barrier region in the week before the mainshock.

We suggest that the anomalous properties of the foreshock zone (compared with the mainshock regions) are the result of fluid circulation within the transform-fault domain. Candidate mechanisms for explaining the velocity-strengthening frictional behaviour and potentially some portion of the large S–P times in the swarm regions are: alteration of the fault zone to serpentine, talc

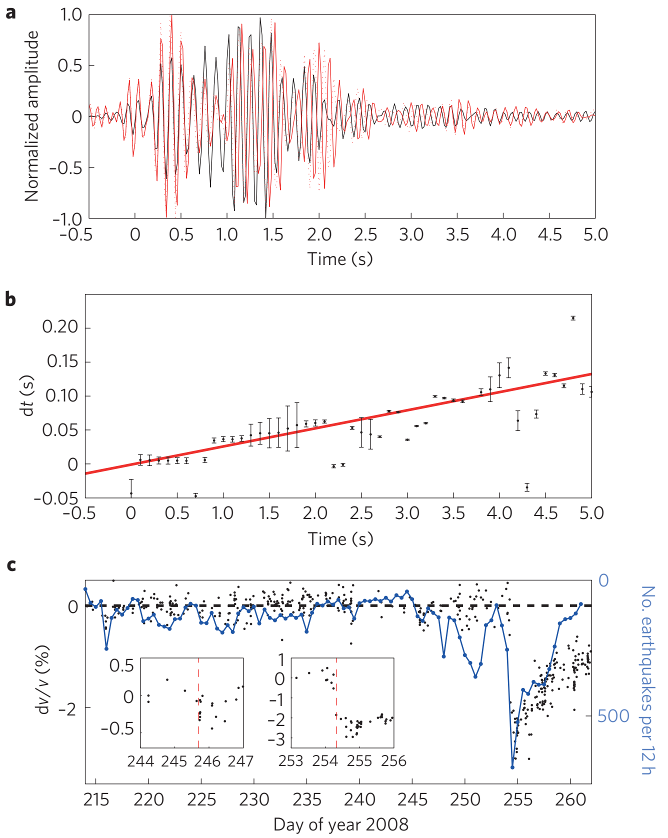

Figure 4 | Temporal velocity changes. a, A comparison of the reference stack of aligned S waveforms at G08 (black line) with a single event on day 255 (red line) and that waveform corrected for the measured dv/v (−2.76%; dotted red line). **b**, Measured $dt(t)$ relative to the reference trace for the day 255 earthquake waveform in **a**. The best-fit slope is a measurement of $-dv/v$. **c**, dv/v measurements (black dots) for a cluster of 439 earthquakes located in the foreshock zone. Insets show the rapid velocity variations around days 245 and 254. The blue curve denotes the earthquakes rate in the region that includes the earthquakes used to measure the velocity changes.

or other hydrous phases; and unusually high porosity and/or fluid pressures in this region. A ~10-km-long serpentine body along the Garrett transform fault[19] provides an example of the along-strike compositional variations that can be expected along EPR transform faults. If present in large quantities, serpentine would produce a V_p/V_s ratio of ~2.0, possibly explaining a portion of the difference in S–P times[20] and thus much of the apparent along-strike variations in the depth extent of seismicity. However, the volume of serpentine that would be required to explain the low P-wave speed anomaly observed in the fault zone is incompatible with the local gravity field[14]. Moreover, our data indicate an ordinary V_p/V_s ratio in the lower crust (see Supplementary Methods and Fig. S4). A thin, undetected layer of serpentine along the fault zone could inhibit earthquake generation. However, although serpentine is velocity strengthening in standard laboratory friction experiments, it becomes velocity weakening at seismic-slip velocities[21] and hence may not provide an explanation for the rupture barrier.

Rather, we interpret the low P-wave velocities at seismogenic depths (3–6 km) in the Gofar foreshock zone[14] to result from high porosity[13], possibly reaching a few per cent in the lower crust[14]. If this zone of enhanced porosity corresponds to a region of pore pressures in excess of hydrostatic, the V_p/V_s ratio could rise to a level required[20] to explain a fraction of the large S–P times. Although this effect could explain some of the along-strike variations in maximum

S–P time seen in Fig. 3, our analysis of the V_p/V_s ratio indicates that the large range in hypocentral depths within the foreshock region is real (see the Supplementary Discussion). Near-lithostatic pore pressures in the lower crust within a narrow region of the active fault zone would enable the fault to fail aseismically in slow earthquakes[22], potentially explaining the ability of the foreshock region to stop large ruptures. Alternatively, the hydrological conditions in the barrier region may favour dilatancy strengthening and thus prevent the propagation of large ruptures[23]. The temporal variations of porosity resulting from dilatancy closely track the history of strain rate (not stress) in the shear zone[23]. If the slow earthquake on days 254–262 caused an increase in porosity over a portion of the fault zone that is sufficiently wide (~200–500 m) for the coda waves to detect it, this would explain the unexpected correlation between seismicity rate (for example stress rate not stress) and wave-speed reductions (Fig. 4). The high porosity of the Gofar foreshock zone contrasts with the seismogenic zone of the Clipperton transform fault where a similar refraction study did not find evidence of a large decrease in P-wave speed in the lower crust[24]. M ~6.6 earthquakes occur regularly[8] in that part of the Clipperton fault, indicating that the presence or absence of a high-porosity damage zone at seismogenic depths may be the primary control on whether large ruptures propagate through a particular segment of an RTF.

Although their relative contribution is not resolved by our data, it is likely that enhanced cooling, serpentinization and high fluid pressure combine to produce the apparently greater depth extent of seismicity and the velocity-strengthening behaviour of the 2008 foreshock region. These mechanisms all point to enhanced fluid circulation in the foreshock region relative to the portions of the fault that fail in large earthquakes. Given that velocity-strengthening regions such as the foreshock zone predominate on the 10,000+ km of faults in the global transform system[3,6], we suggest that the fluid-related effects may be as dominant as thermal effects in controlling earthquake rupture on oceanic faults.

Methods

We constructed an initial earthquake catalogue covering the calendar year of 2008 using standard short-term average to long-term average (STA/LTA)-based detection algorithms for P waves and wavelet-based detections[25] for S-wave arrival times. However, owing to the very low-amplitude P-wave arrivals on OBSs and the short temporal separations between P and S waves, these algorithms missed many arrivals. To overcome this limitation, we used the best located events from the STA/LTA catalogue to provide waveform templates for a matched filter-based detection algorithm similar to that of Peng[26] (see Supplementary Methods).

A subset of 21,919 earthquakes between August and December 2008 from the waveform-derived catalogue were used in the relative relocations. These events had detections on at least six stations and they were retained by the hypoDD relocation programme's[27] clustering algorithm, requiring at least seven differential time observations per pair with a cross-correlation cutoff of ≥ 0.75. Differential arrival times were calculated using a time-domain interpolation algorithm[28] and resulted in a significant (~0.2 s) improvement over first-arrival picks (Supplementary Fig. S6). A window of 2.56 s around each arrival was extracted from the waveform database, tapered and filtered. S waves were bandpass filtered between 5 and 12 Hz whereas P waves were filtered between 5 and 15 Hz. In general, the broadband channels were used for the correlation except for a period of 3–9 days following the M 6.0 earthquake when they were not functioning due to clipping/relevelling problems. On these days, the accelerometer components were used. The relocations were done in three subsets by longitude, 106.40° W–106.00° W, 106.04° W–105.90° W and 105.94° W–105.50° W. For the eastern and western sections, we required six observations per pair, whereas for the middle section we required eight observations per pair owing to denser instrumentation and higher seismicity rates in this region. For the three groups, we used 1.9 million, 0.7 million and 0.6 million P and 3.7 million, 1.9 million and 3.7 million S differential arrival time measurements to relocate 10,779, 9,462 and 6,258 earthquakes, respectively. For earthquakes in the regions of overlap, we used the location estimate from the middle relocation with stricter criteria. We did not use catalogue arrival times owing to their significantly higher percentage of mis-identified phases. We used a one-dimensional version of the P-wave velocity model of Roland[14] that accounts for the significant (~20–30%) reductions in P-wave speeds in the Gofar fault zone relative to ordinary EPR crust. We assumed a V_p/V_s ratio of 1.73. Experiments were carried out to verify the depth extent of the relocated seismicity (see Supplementary Methods).

The dv/v of the S-wave velocity during the foreshock sequence is measured using the doublet method[29]. This method measures time shifts dt between a waveform and a reference trace, as a function of the time t in the record. Here we selected foreshocks with waveforms as recorded at station G08 similar to a master event and contained within a cluster ~1 km long in the along-strike direction, and used a stack of those occurring before day 240 as a reference trace. For each of the 439 selected foreshocks and each of the three broadband and the three accelerometer components, the waveform is compared with the reference trace using a tapered, one-second-long, moving time window centred on t to measure dt as a function of t. This is done in two different frequency bands (5–8 Hz and 8–12 Hz). Although this method works well for small dv/v, when velocity variations are as high as 3%, as measured here, the same time windows for the reference and the present event do not correspond to the same cycles in the waveform (especially for large values of t) and dt cannot be measured. To overcome this limitation, we first determine a coarse stretching coefficient ε (which is an approximate value for dt/t) using the stretching method[30] and use it to define the centre of the time window for the selected event in the doublet method as $(1+\varepsilon)t$ instead of t. A stretching coefficient dt/t is then inferred using a linear regression to fit dt as a function of t (Fig. 4 middle). Assuming a homogeneous velocity variation dv/v, then dt/t is equal to the opposite of the relative change in S-wave velocity $-dv/v$ between the (arbitrary) reference and the event date. The resulting dv/v estimates are of similar amplitude on the six components and the two frequency bands we used (within 10%—see Supplementary Fig. S7), which gives confidence that they are not biased by any coupling resonance issues. Measurements on the six components and the two frequency bands are then averaged to increase the accuracy on dv/v. Repeating this process for each event of the dense foreshock sequence allows for a continuous monitoring of S-wave velocity variations from day 215 to day 262 when the main shock occurred (Fig. 4c).

Received 13 December 2011; accepted 21 March 2012; published online 22 April 2012

References

1. Boettcher, M. S., Hirth, G. & Evans, B. Olivine friction at the base of oceanic seismogenic zones. *J. Geophys. Res.* **112,** B01205 (2007).
2. Abercrombie, R. E. & Ekstrom, G. Earthquake slip on oceanic transform faults. *Nature* **410,** 74–77 (2001).
3. Boettcher, M. S. & Jordan, T. H. Earthquake scaling relations for mid-ocean ridge transform faults. *J. Geophys. Res.* **109,** B12302 (2004).
4. Bird, P., Kagan, Y. Y. & Jackson, D. D. in *Plate Boundary Zones* Vol. 30 (eds Stein, S. & Freymueller, J. T.) 203–218 (Geodynamics Series, AGU, 2002).
5. Roland, E., Behn, M. D. & Hirth, G. Thermal–mechanical behavior of oceanic transform faults: Implications for the spatial distribution of seismicity. *Geochem. Geophys. Geosyst.* **11,** Q07001 (2010).
6. Brune, J. N. Seismic moment seismicity and rate of slip along major fault zones. *J. Geophys. Res.* **73,** 777 (1968).
7. McGuire, J. J. Seismic cycles and earthquake predictability on East Pacific Rise transform faults. *Bull. Seismol. Soc. Am.* **98,** 1067–1084 (2008).
8. Boettcher, M. S. & McGuire, J. J. Scaling relations for seismic cycles on mid-ocean ridge transform faults. *Geophys. Res. Lett.* **36,** L21301 (2009).
9. McGuire, J. J., Boettcher, M. S. & Jordan, T. H. Foreshock sequences and short-term earthquake predictability on East Pacific Rise transform faults. *Nature* **434,** 457–461 (2005).
10. Searle, R. C. Multiple, closely spaced transform faults in fast-slipping fracture-zones. *Geology* **11,** 607–610 (1983).
11. Roland, E. & McGuire, J. J. Earthquake swarms on transform faults. *Geophys. J. Int.* **178,** 1677–1690 (2009).
12. Kaneko, Y., Avouac, J. P. & Lapusta, N. Towards inferring earthquake patterns from geodetic observations of interseismic coupling. *Nature Geosci.* **3,** 363–369 (2010).
13. Korenaga, J., Kelemen, P. B. & Holbrook, W. S. Methods for resolving the origin of large igneous provinces from crustal seismology. *J. Geophys. Res.* **107,** 2178 (2002).
14. Roland, E. *Earthquake Behavior and Structure of Oceanic Transform Faults* PhD thesis, Massachusetts Institute of Technology (2011).
15. Silver, P. G., Daley, T. M., Niu, F. & Majer, E. L. Active source monitoring of cross-well seismic travel time for stress-induced changes. *Bull. Seismol. Soc. Am.* **97,** 281–293 (2007).
16. Dieterich, J. A constitutive law for rate of earthquake production and its application to earthquake clustering. *J. Geophys. Res.* **99,** 2601–2618 (1994).
17. Rivet, D. *et al.* Seismic evidence of nonlinear crustal deformation during a large slow slip event in Mexico. *Geophys. Res. Lett.* **38,** L08308 (2011).
18. Lohman, R. B. & McGuire, J. J. Earthquake swarms driven by aseismic creep in the Salton Trough, California. *J. Geophys. Res.* **112,** B04405 (2007).
19. Hekinian, R., Bideau, D., Cannat, M., Francheteau, J. & Hebert, R. Volcanic activity and crust mantle exposure in the ultrafast garrett transform-fault near 13-degrees-28S in the Pacific. *Earth Planet. Sci. Lett.* **108,** 259–275 (1992).

20. Christensen, N. I. Pore pressure and oceanic crustal seismic structure. *Geophys. J. R. Astron. Soc.* **79,** 411–423 (1984).
21. Kohli, A. H., Goldsby, D. L., Hirth, G. & Tullis, T. Flash weakening of serpentinite at near-seismic slip rates. *J. Geophys. Res.* **116,** B0302 (2011).
22. Liu, Y. J. & Rice, J. R. Slow slip predictions based on granite and gabbro friction data compared to GPS measurements in northern Cascadia. *J. Geophys. Res.* **114,** B09407 (2009).
23. Samuelson, J., Elsworth, D. & Marone, C. Influence of dilatancy on the frictional constitutive behavior of a saturated fault zone under a variety of drainage conditions. *J. Geophys. Res.* **116,** B10406 (2011).
24. Van Avendonk, H. J. A., Harding, A. J., Orcutt, J. A. & McClain, J. S. A two-dimensional tomographic study of the Clipperton transform fault. *J. Geophys. Res.* **103,** 17885–17899 (1998).
25. Simons, F. J., Dando, B. D. E. & Allen, R. M. Automatic detection and rapid determination of earthquake magnitude by wavelet multiscale analysis of the primary arrival. *Earth Planet. Sci. Lett.* **250,** 214–223 (2006).
26. Peng, Z. G. & Zhao, P. Migration of early aftershocks following the 2004 Parkfield earthquake. *Nature Geosci.* **2,** 877–881 (2009).
27. Waldhauser, F. & Ellsworth, W. L. A double-difference earthquake location algorithm: Method and application to the northern Hayward fault, California. *Bull. Seismol. Soc. Am.* **90,** 1353–1368 (2000).
28. Schaff, D. P. *et al.* Optimizing correlation techniques for improved earthquake location. *Bull. Seismol. Soc. Am.* **94,** 705–721 (2004).
29. Poupinet, G., Ellsworth, W. L. & Frechet, J. Monitoring velocity variations in the crust using earthquake doublets—an application to the Calaveras fault, California. *J. Geophys. Res.* **89,** 5719–5731 (1984).
30. Sens-Schonfelder, C. & Wegler, U. Passive image interferometry and seasonal variations of seismic velocities at Merapi volcano, Indonesia. *Geophys. Res. Lett.* **33,** L21302 (2006).

Acknowledgements

We would like to thank the W. M. Keck Foundation for the financial support to build the OBSs that carried strong-motion accelerometers and made this study possible. We thank the crews of the RVs *Thomas G. Thompson*, *Marcus Langseth* and *Atlantis* for three nearly flawless cruises needed to collect this data set. We thank the Woods Hole Oceanographic Institution Ocean Bottom Seismic Instrumentation Pool group, K. Peal, R. Handy, A. Gardner, D. Dubois, D. Kot, P. Lemmond and J. Ryder, for collecting such an amazing data set. This work was done with the support of the National Science Foundation grant OCE-0242117. P.G. is supported by a Shell research grant.

Author contributions

J.J.M. and J.A.C. conceived the OBS experiment. J.J.M., J.A.C., M.S.B. and E.R. participated in the three research cruises and associated data collection. J.J.M. and J.A.C. derived the earthquake catalogue. P.G. and R.D.v.d.H. carried out the velocity-change analysis. E.R. and D.L. determined the seismic velocity model used for relocations. E.R. and M.D.B. carried out the thermal modelling. All authors discussed results and contributed to the manuscript.

Additional information

The authors declare no competing financial interests. Supplementary information accompanies this paper on www.nature.com/naturegeoscience. Reprints and permissions information is available online at www.nature.com/reprints. Correspondence and requests for materials should be addressed to J.J.M.